LASER INTERFEROMETER GRAVITATIONAL WAVE OBSERVATORY
- LIGO -
CALIFORNIA INSTITUTE OF TECHNOLOGY
MASSACHUSETTS INSTITUTE OF TECHNOLOGY

Document Type LIGO-T980021-00 - D

Measurement of Self-induced Beam Effects in Transmissive Optics for LIGO

Sanichiro Yoshida, Efim Khazanov, Oleg Kulagin, Justin Mansell, Alexandre Gorlenko, Dave Reitze, Rana Adhikari, Tom Delker, Qi-Ze Shu, Guido Mueller and David Tanner

Distribution of this document:

IOO Design Review Board

This is an internal working note
of the LIGO Project.

California Institute of Technology
LIGO Project - MS 51-33
Pasadena CA 91125
Phone (818) 395-2129
Fax (818) 304-9834
E-mail: info@ligo.caltech.edu

Massachusetts Institute of Technology
LIGO Project - MS 20B-145
Cambridge, MA 01239
Phone (617) 253-4824
Fax (617) 253-7014
E-mail: info@ligo.mit.edu

WWW: http://www.ligo.caltech.edu/

1 INTRODUCTION

In this document we discuss the high power effect on IOO optics. Specifically, we discuss thermal lensing effects in the Faraday rotator (FR) and Electro-Optical Modulator (EOM) induced by high power laser beams, polarization contamination caused by thermally induced birefringence in the FR and EOM, and RFAM generated by the EOM.

2 SUMMARY

Table 1 compares the results of the measurement with the requirement.

Table 1: Summary of measurement

item	*requirement*	*measurement*
TEM_{00} Power loss due to FR thermal lens	5%	3%
FR polarization	100:1	170:1
FI isolation	-35 dB	<-36 dB
EOM residual intensity modulation	1×10^{-3}	$<2.5 \times 10^{-6}$
Alignment tolerance	4.3 deg	0.02 deg

3 FARADAY ISOLATOR

3.1. Requirements

3.1.1. Power coupling

SYS requires that the light from the PSL be coupled into the COC with 95% efficiency. When the TGG crystal of the FR is exposed to high power YAG radiation, it behaves as a focusing lens due to thermal lensing. This changes the wavefront of the YAG laser beam traveling toward the mode matching telescope and thereby degrades the coupling efficiency. This wavefront distortion cannot be corrected by the mode cleaner (MC) because the FR is placed after the MC. Our previous theoretical estimation indicates that at 10 W YAG input the effective focal length of this thermal lens is about 60 m and causes 1% power decoupling [1]. SYS also requires that TEM_{mn} field (n, m>0) be 0.001 of TEM_{00}. Thermal lensing will introduce higher order modes since the optical path difference is not spherical.

3.1.2. Polarization

Depolarization is required to be less than 100:1 [2]. The TGG crystal is a cubic crystal and is originally optically isotropic. However, when it is exposed to high power radiation, the thermal

stress can generate birefringence and cause depolarization. In this test, we measure depolarization as a function of the YAG power.

3.1.3. Isolation

According to Ref. [3], the isolation is required to be at the level of -70 dB by two Faraday isolators (FI), implying that the isolation level of one FI must be better than -35 dB. In this test, we assess the isolation ratio by measuring the double-pass depolarization of the FR.

3.2. Measurements

3.2.1. Thermal Lensing/Mode Quality

Figure 1shows the experimental set up for the thermal lensing measurement.We evaluated thermal lensing by measuring the thermally induced change in the optical path length (OPL) as a function of r, where r is the radial coordinate axis of a plane perpendicular to the optical path. To measure the change in OPL (ΔOPL), we used a Shack-Hartman wavefront detector (SHWD, manufacturer: WaveFront Sciences, Inc.).We employed a pump and probe type arrangement for this measurement. The probe laser was a He/Ne laser (Melles Griot, model 05-LLR-811-249) and the pump laser was a 10 W YAG (Lightwave model 220-1064-10000). The pump and probe geometry was selected for two reasons. First, SHWD has higher sensitivity at 633 nm. Second, power balancing to ensure constant intensity on the SHWD was not necessary using the He/Ne laser. The probe laser beam was introduced to the FR collinearly with the 10 W YAG. M3 and M4 are dichroic mirrors that pass the He/Ne laser wavelength but reflect the YAG wavelength. The reflected pump beam was measured by a power meter. The 10 W YAG laser's output was transmitted through a polarizer (CVI, cubic polarizer PBSC) to purify the polarization.

Figure 1: Experimental arrangement for thermal lensing measurement

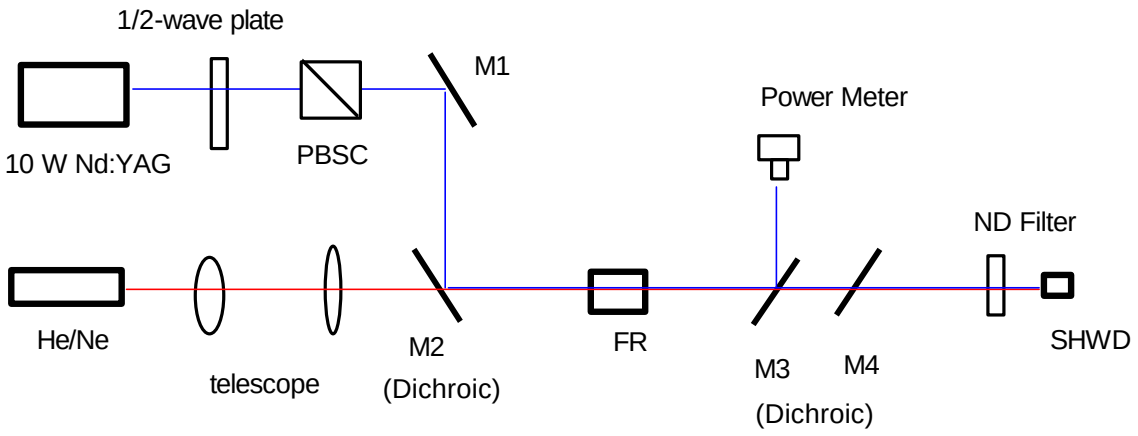

The measurement was carried out for the FR manufactured by Electro-optics Technology, Inc. (EOT). To simulate the actual situation where the YAG beam is affected by the thermal lens created by itself, we set the radii of the pump and probe beams as close as possible to each other. For this purpose, we expanded the He/Ne beam by a telescope. The waist sizes of the He/Ne laser

and the YAG laser measured at the location of the FR were, respectively, 1.79 mm and 1.62 mm. This YAG waist size is the same as the waist size in the mode cleaner of the 4K LIGO.

Figure 2. shows the thermal lensing observed at various YAG powers as a function of radial distance from the center of the thermal lens, r, normalized by the YAG waist size, w_{YAG}. The data were obtained by averaging the change in OPL (ΔOPL) measured for the same r over 360 degree around the center of the thermal lens. By this averaging, the influence of the probe laser's beam wandering (beam tilt at the SHWD's image plane) can be reduced. In our data, the ΔOPL measurements are referenced to the center of the beam.

Figure 2: Thermal lensing in FR (EOT) at various YAG powers

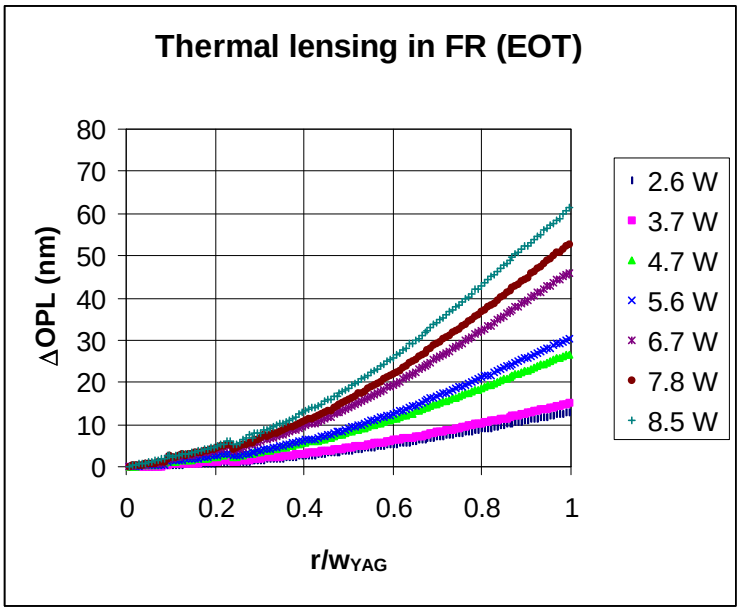

In order to confirm that the observed ΔOPL is purely due to the thermal lensing effect caused by the YAG beam, we carried out the same measurement with a different probe laser diameter and the YAG laser diameter unchanged. To reduce the probe laser radius, we removed the telescope from the setup shown in Figure 1. This reduced the probe laser beam diameter by a factor of two. Figure 3 shows the observed ΔOPL as a function of YAG laser power at various YAG laser's radii, and compare them with Figure 2. In Figure 3, open plots represent the case when the probe (He/Ne) laser has the same radius as the YAG laser and solid plots represent the case when the probe laser' radius is about a half of the YAG laser. If ΔOPL is purely caused by the thermal lensing, its power dependence should vary depending on the YAG laser radius but independent of the probe laser radius. Figure 3 clearly indicates that this is the case.

Figure 3: ΔOPL at various YAG waists. Open plots are the case when $w_{He/Ne}=w_{YAG}$, solid plots are the cases when $w_{He/Ne}=1/2w_{YAG}$

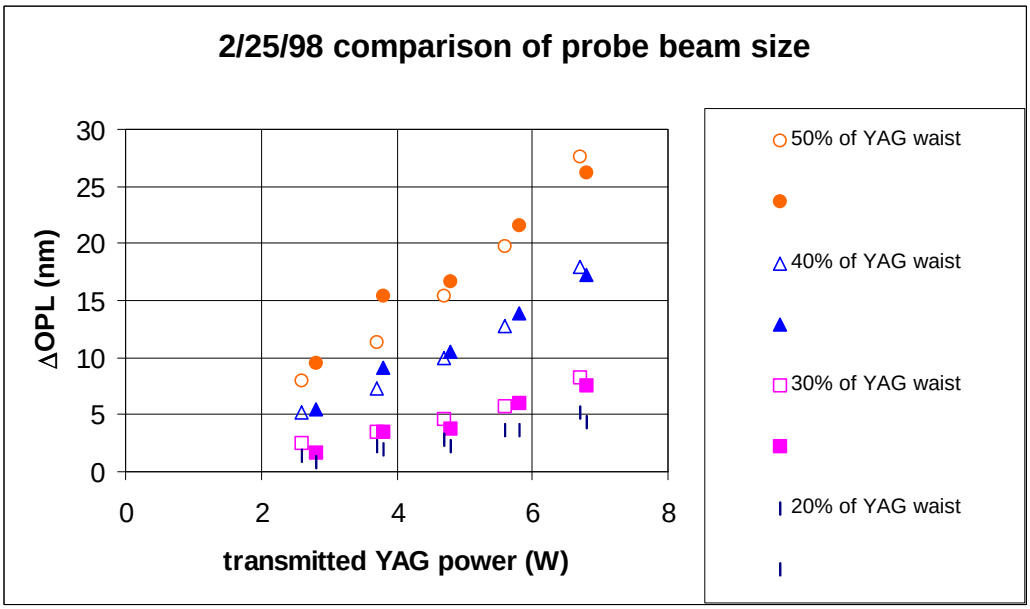

When the absorption is uniform and the heated sample's diameter is much larger than the heating beam, ΔOPL caused by the temperature distribution in the sample can be approximated by the following equation [4].

$$\Delta OPL(r) = 0.07741 \cdot \frac{P_{abs} \cdot L}{k_{th}} \left[\frac{dn}{dT} + \alpha \cdot n\right] \left[\frac{r^2}{w^2} + 0.4 \cdot \frac{r}{w}\right] \quad (1)$$

where P_{abs} is the power absorbed in the unit length, k_{th} is the thermal conductivity, n is the refractive index, L is the length of the crystal, r is the radial coordinate, α is the thermal expansion coefficient and w is the beam waist. This equation indicates that at a fixed r/w, ΔOPL increases linearly in proportion to the absorbed power, hence transmitted power. This explains the linearity seen in Figure 3. In Figure 4, we plot ΔOPL observed at the YAG waist as a function of transmitted YAG power. Because of the approximate linearity, this graph can be used to predict ΔOPL at higher powers. Also shown in Figure 4 are the results of the same ΔOPL measurement for a TGG rod of the same size without placing it in the FR magnet housing, and theoretical ΔOPL at the YAG waist calculated by eq. (1) with the numbers shown below. The ΔOPL measured for the TGG rod placed in the FR magnet housing appears to be higher than the TGG only case and the theory. This discrepancy is not completely understood, but is possibly due to a change in thermal conductivity owing to the presence of the magnet and housing.

Table 2: Constants used to calculate in ΔOPL TGG

absorption coefficient (cm^{-1})	*thermal conductivity (W/mK)*	*refractive index*	*thermal expansion coefficient*	*crystal length (cm)*	*dn/dT (1/K)*
1.5×10^{-3}	7.4	1.95	9.4×10^{-6}	2	2×10^{-5}

Figure 4: OPL change at YAG waist

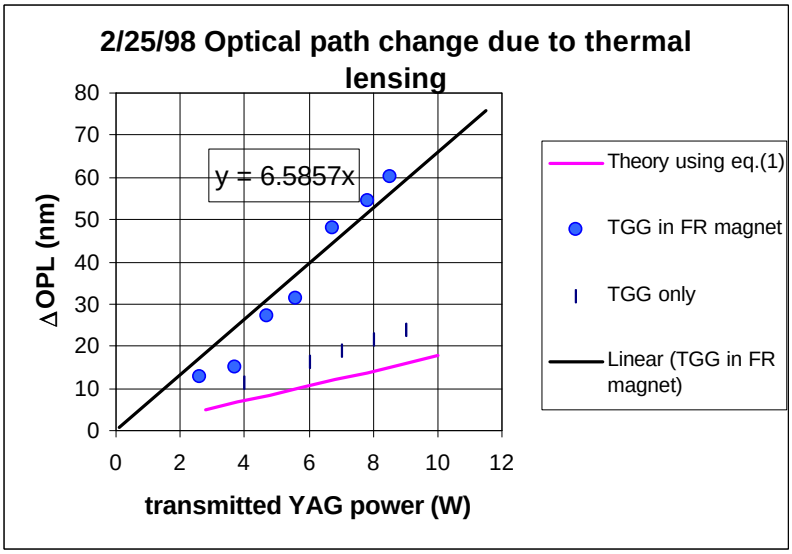

We next estimate the effective focal length of the observed thermal lens and compare it with the focal length that we calculated in PDR. To evaluate the effective radius of curvature of the thermal lens, we curve-fitted the observed ΔOPL to $\Delta OPL=r^2/2F$, where r is the radial distance from the thermal-lens-center and F is the effective focal length of the thermal lens. Since the w_{YAG} is the same as the actual beam radius of the 4K LIGO, the effective focal length obtained here represents the actual thermal lens of the 4K system. We next extrapolated Figure 4 on its YAG power axis to estimate ΔOPL at laser power higher than the maximum measured YAG power of 8.5 W. Using the value of ΔOPL determined in this a way and the formula $\Delta OPL=r^2/2F$, where r=1.62 mm, we evaluated F at several YAG laser powers.Figure 5 compares the effective focal length estimated in these fashions with the focal length calculated in PDR. Figure 5 also compares the effective focal length estimated by the ΔOPL measured using the TGG rod only (Figure 4). The effective focal lengths based on the curve fitting and those estimated by the above-mentioned extrapolation show good agreement with each other, and both are smaller than the calculation in PDR by a factor of 2. Since the effective focal length for the TGG only case shows reasonable agreement with the calculation, this factor of two discrepancy is possibly due to the change in thermal conductivity as discussed in Figure 4. Nevertheless, the presently estimated thermal lensing for the FR corresponds to power coupling loss of 3%. This is within the range of requirement, and can be improved by repositioning of the MMT mirrors 1, 2 (see IOOFDD).

Figure 5: Effective focal length of thermal lens

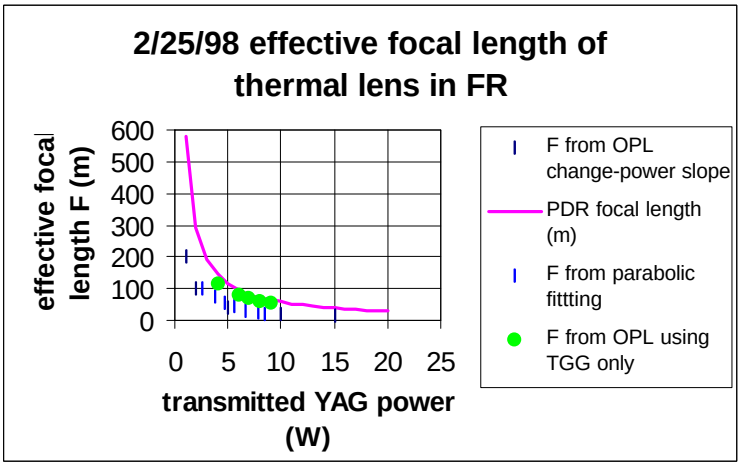

3.2.1.1 Polarization

We first measured the one-pass depolarization of the FR. Figure 6 shows experimental setup for this measurement. This arrangement works in the following way. Polarizer 1 purifies the vertical polarization of the YAG laser output-beam (initially 100:1). By passing through the FR, the polarization rotates by 45 deg. Halfwave plate 2 rotates this polarization back to vertical. Polarizer 2 passes the horizontal polarization through to a photo-diode and reflects the horizontal polarization to a power meter. Thus by measuring the power transmitted through polarizer 2, P_t, and comparing it with either the initial power P_i or reflected power P_r, the depolarization can be evaluated. Table 3 lists the extinction ratios of the polarizers.

Table 3: Extinction ratio of polarizers

	polarizer 1	*polarizer 2*
Manufacturer, model	CVI, PBSC x 2	CVI, CPAD
extinction ratio	4×10^4:1	5×10^5:1

Note: We used two identical polarizers in series for Polarizer 1 to improve the extinction ratio.

The following measurements were made.

- Power dependence of depolarization in TGG (no magnetic field)
- Power dependence of depolarization in TGG (magnetic field present)
- Temperature dependence of depolarization in TGG (magnetic field present)
- Orientation dependence of depolarization in TGG (magnetic field present)

Figure 6: Experimental arrangement for measurement of depolarization in FR and TGG rod

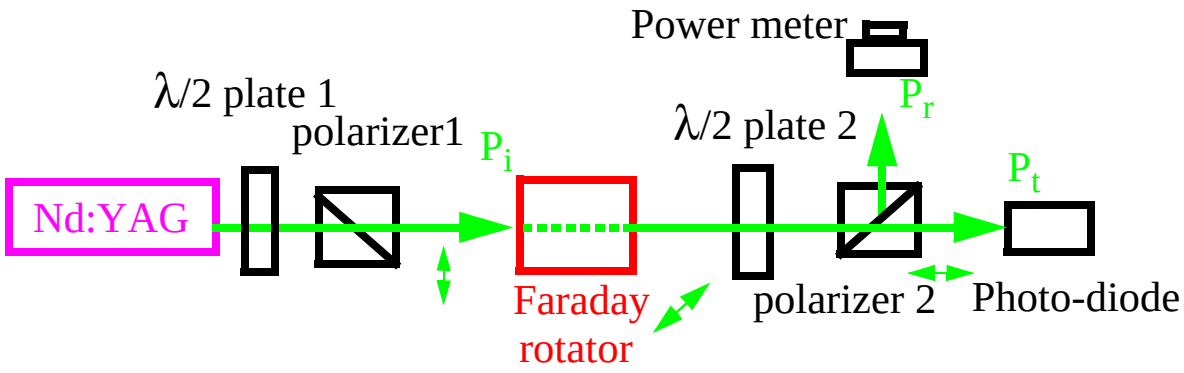

3.2.1.1.1 TGG rod

As a baseline, we first measured depolarization of the TGG rod only (manufactured by EOT). In this measurement, we did not use polarizer 2 because the polarization does not rotate. The result is shown inFigure 7, where depolarization P_t/P_i is plotted as a function of P_i. Solid circles show P_t/P_i measured without the TGG rod, i.e., the background noise level of the setup. The measured depolarization shows clear quadratic dependence on P_i. This indicates that the observed depolarization is due to birefringence of the TGG crystal caused by the thermal load of the YAG laser for the following reason. When a TGG crystal is exposed to high power laser radiation, birefringence is induced by the photoelastic effect. This generates a phase retardation δ that can be written as follows [5].

$$\delta = \frac{2\pi}{\lambda} L(\Delta n_\phi - \Delta n_r) = (n_0)^3 \frac{\alpha Q}{\kappa} C_B r^2 \qquad (2)$$

where is λ the wavelength, L is the crystal length, Δn_ϕ and Δn_r are the refractive indices along the radial axis (r) and the tangential axis (ϕ), n_0 is the initial refractive index, α is the thermal expansion coefficient, Q is the absorbed power density and C_B is a material constant determined

by the Poisson's ratio and photoelastic tensor components, and r is the radius. Since the absorbed power is proportional to the incident power P_i, δ is proportional to P_i. The depolarization can be expressed as

$$\left(\frac{E_h}{E_0}\right)^2 = \sin^2 2\theta \cdot \sin^2\frac{\delta}{2} \approx \frac{\delta}{2} \cdot \sin^2 2\theta \qquad (3)$$

where E_h is the amplitude of the horizontal polarization (relative to the optical table) transmitted through polarizer 2, θ is the angle between the polarization and the fast axis, and we have assumed $\delta << 1$. The linear dependence on δ of the depolarization gives rise to the quadratic dependence on power.

Figure 7: Depolarization in TGG crystal (EOT)

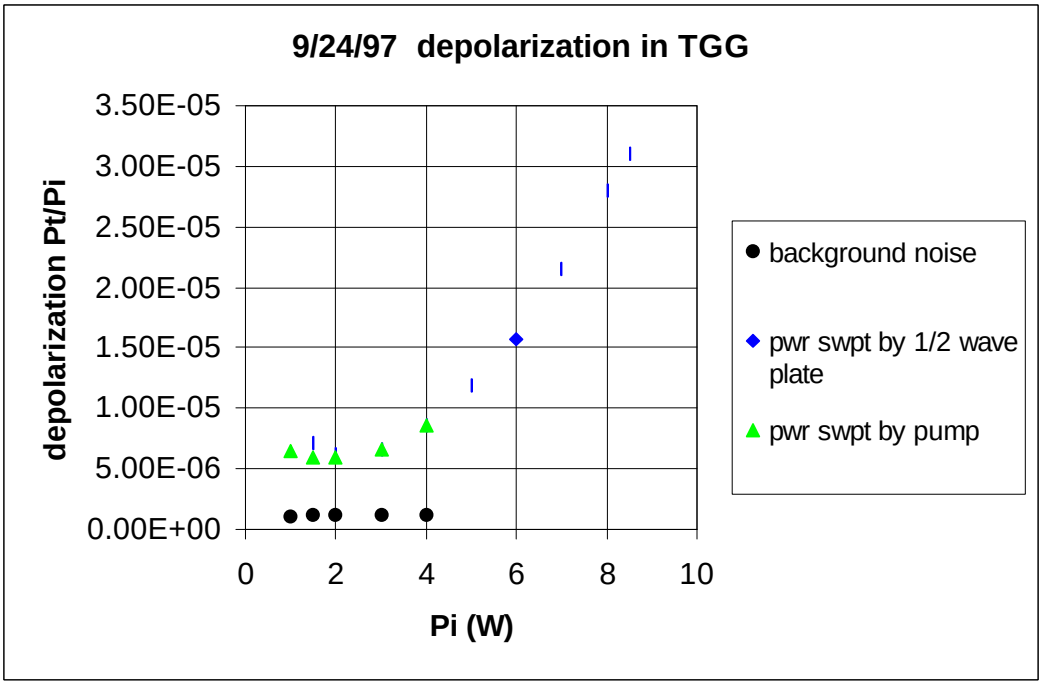

3.2.1.1.2 Faraday rotators

Next we measured the depolarization of FRs manufactured by EOT and Synoptics. The results for the EOT FR are shown in Figure 8. An order of magnitude higher depolarization than the case of the TGG crystal only is seen. However, this is smaller than the required extinction ratio of 35 dB. Note that in these measurements, we used $\lambda/2$ plate 2 and part of the observed depolarization is due to the insertion of this half wave plate. We did not optimized the translational or rotational position of the FR with respect to the laser beam. The fact that the depolarization does not depend

on P_i indicates that the dominant factor for the depolarization is not thermally induced birefringence but other factors such as the laser beam passed through where the TGG crystal has intrinsic depolarization and/or the B-field is not uniform.

Figure 8: Single-pass depolarization of EOT FR

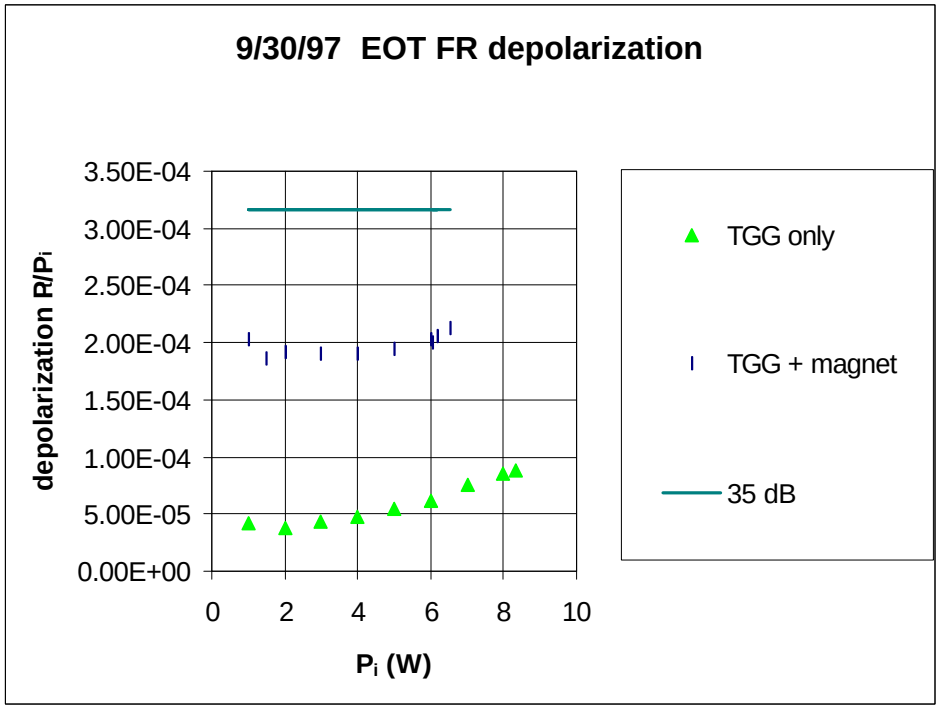

3.2.1.1.3 Temperature dependence

We also investigated the change in polarization state with temperature. The temperature dependence of the Verdet constant of the TGG results in change in the output polarization state given by eq. (4).

$$d\Theta = \frac{dV}{dT} \cdot dT \int H dz \qquad (4)$$

where Θ is the rotation of polarization by a FR, V is the Vert constant, T is the temperature, H is the magnetic field and z is the coordinate axis along the optical path. For the temperature dependence of the Verdet constant, we used dV/dT=-0.00526V [6]. To evaluate the integral appearing on the right-hand side of eq. (4), we assumed that Θ was initially 45 deg.

The experimental procedure was as follows. We first optimized the angle of λ/2 plate 2 and other optical components so that the single-pass depolarization was minimized. We then varied the temperature of the TGG crystal slowly so that the crystal was in quasi-thermal-equilibrium at all times. When the increase in P_t became substantial, we rotated λ/2 plate 2 in such a way that P_t was minimized and recorded the angle of this rotation. We repeated this until the overall temperature difference was 10 °C . Figure 9 shows the result of this experiment where we plot the angle of the rotation of λ/2 plate 2 as a function of the measured room temperature change, and compare it with theoretical relationship based on eq. (4).

Figure 9: . Temperature dependence of FR performance (EOT)

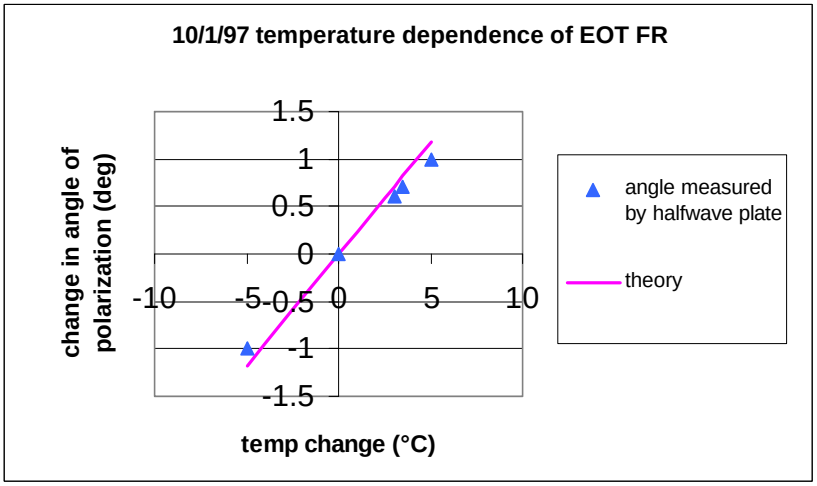

In Figure 10, the influence of temperature change is represented in terms of the depolarization. From our measurement *we find that the temperature change must be less than ± 3 deg to ensure 35 dB isolation.*

Figure 10: Change in depolarization due to temperature change

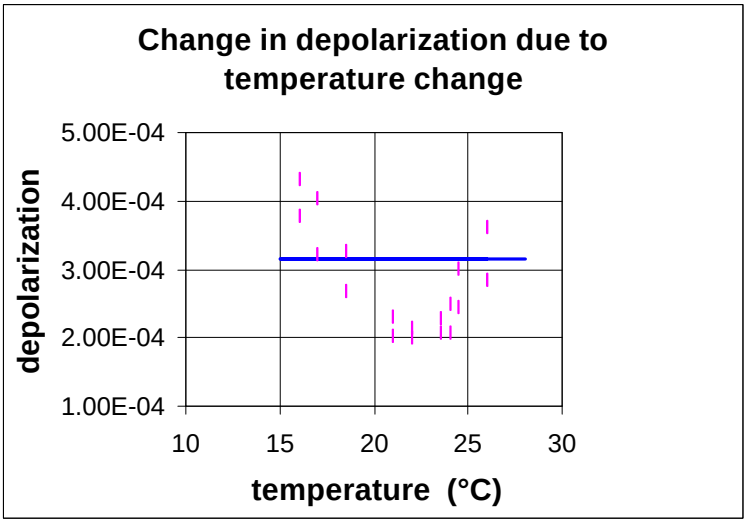

3.2.1.1.4 Orientational dependence of TGG depolarization

When thermally stressed by laser radiation, it is expected that the TGG rod is more resistive along the crystallographic axes than in other directions, and therefore thermally induced strain is smaller along the crystallographic axes. This indicates that the thermally induced depolarization should depend on the angle between the polarization and the TGG's crystallographic axes, i.e., when the polarization is in parallel to one of the crystallographic axes, the depolarization will be smaller than the case when the polarization is in a direction between the two axes. Thus we measured the dependence of the single-pass depolarization on the azimuthal angle of the incident polarization. Figure 11 shows the result. We changed the relative angle between the polarization of the incident beam and the crystallographic axes of the FR by either rotating the incident polarization by a halfwave plate or by rotating the FR about the optical path. In Figure 11, triangle plots represent the case when the FR was rotated and the other plots are the cases when the incident polarization was rotated by the halfwave plate. It is seen that depending on the angle, the depolarization can be different as much as an order of magnitude.

Figure 11: Orientation dependence of EOT FR.

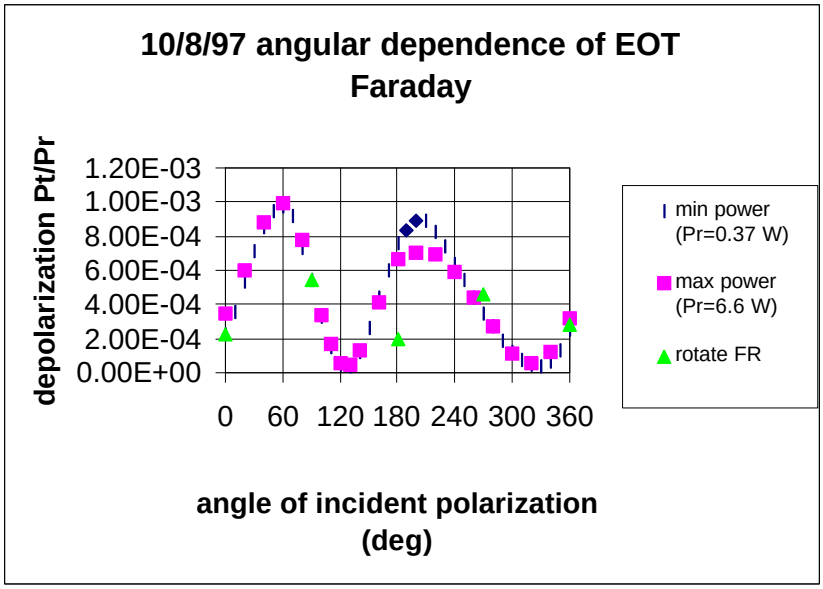

3.2.1.2 Isolation

We next measured double-pass depolarization that defines the isolation ratio.Figure 12 shows the experimental arrangement.We placed a total reflector at the end of the optical path so that the full power would be fed back to the FR. The power returning to the YAG laser passes through FR twice and therefore its polarization is orthogonal to the initial polarization. Thus most of it is reflected by polarizer 1, (P_{2r}), and only the depolarized portion passes through the polarizer (P_{2t}). We measured, P_{2r} by a power meter and, P_{2t} by a beam splitter (uncoated optical wedge) and a photo detector.

Figure 12: Optical arrangement for double-pass isolation measurement

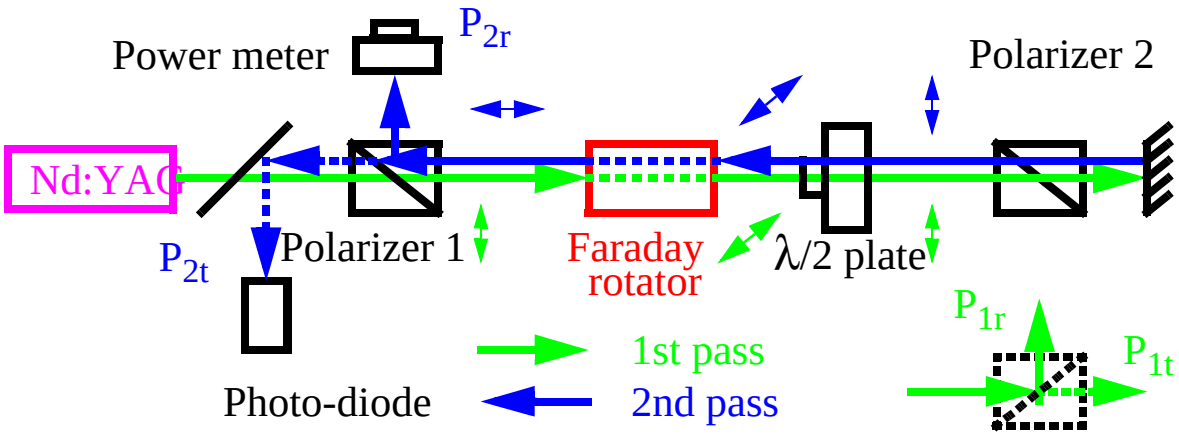

For this measurement, we used the same FR as Figure 8, after baking it at Caltech for a vacuum contamination test. In order to check if the baking degrades the performance, we first measured the single-pass depolarization. We adjusted the angle of the halfwave plate and the translational position of the FR with respect to the laser beam so that the single-pass depolarization might be minimized. The result is shown in Figure 13. No degradation by the baking is observed.

We next measured the double pass depolarization P_{2r}/P_{2r} and defined it as the isolation ratio of the Faraday isolator (FI). For this measurement, we adjusted the angle of the halfwave plate and the translational position of the FR so that the double-pass depolarization might be minimized. The result is shown in Figure 13. The power dependence of the double-pass depolarization appears the same as the single-pass depolarization. At the maximum YAG power of 6.5 W, the isolation ratio is smaller than the targeted value of 35 dB by a factor of two (38 dB).

Figure 13: Double pass isolation of EOT FI

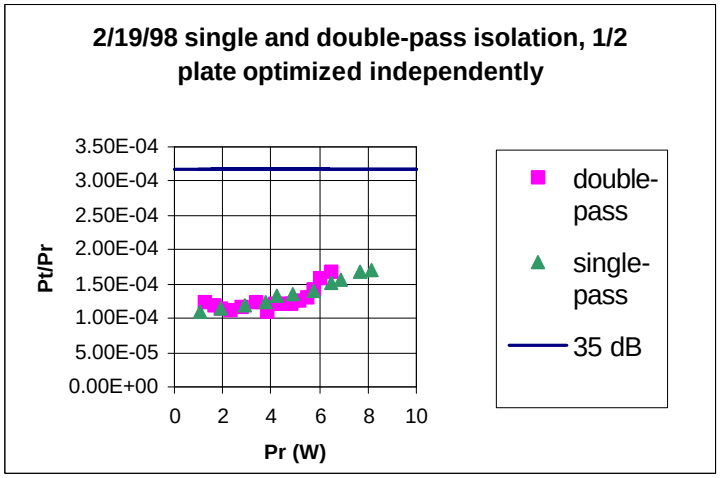

3.2.2. Faraday Isolator Selection (Type, Manufacturer, etc.)

Table 4 lists the specification of the Faraday rotator we have selected.

Table 4: FR specifications

Manufacturer	*Electro-Optics Technology*
Model Number	1845-12
Clear Aperture	12 mm
Transmission @ 1064 nm	>97%
Isolation @ 1064 nm	>30 dB

3.2.3. Polarizer Selection (Type, Manufacturer, etc.)

Table 5 lists the specification of the polarizer we have selected.

Table 5: FR specifications

Manufacturer	*CVI Laser Corp*
Model Number	CPAD-15.0-670-1064
Type	Glan Laser Double Escape Window Polarizer
Extinction ratio	5×10^5:1
Material	Calcite
Transmitted Wavefront	$\lambda/4$ at 633 nm
Antireflection Coating	All entrance and exit surfaces
Housing material	Aluminum
Damage threshold	cw 500 W/cm^2

4 EO MODULATORS

4.1. Requirements

4.1.1. Sideband Stability

4.1.1.1 Resonant SB

A residual amplitude modulation produced in an EOM causes a signal offset at the antisymmetric port. In order to make this offset negligibly small, the residual intensity modulation must be less than 10^{-3} [7]. Since the resonant SB has the largest modulation depth corresponding to the modulation index of 0.5, in this test we evaluate the intensity modulation around this modulation depth.

4.1.1.2 Nonres. SB

Same as Resonant SB.

4.1.1.3 Mode Cleaner

Same as Resonant SB.

4.1.2. Damage Threshold/Thermal Lensing

When the laser beam is introduced to the EOMs, the power clipping must be lower than 10 ppm. For the EOM clear aperture of 2 mm, this corresponds to the beam waist of 0.4 mm. Thus the EOM must tolerate the corresponding power density. Thus in this test, we focus the 10 W YAG laser beam smaller than 0.4 mm and investigate if the $LiNBO_3$ crystal gets damaged.

4.1.3. Alignment Tolerance

The alignment between the angles of the EOM's axis and the incident polarization/the polarizer must be small enough to make the residual intensity modulation caused by RFAM be lower than the required value of $1x10^{-3}$ [7]. The next table shows the corresponding alignment tolerance.

Table 6: Alignment tolerance

required RFAM (in intensity modulation)	*alignment tolerance*
1×10^{-3}	4.3 deg

4.2. Testing Results

4.2.1. Sideband Stability

Figure 14 shows the experimental arrangement for the measurement of the residual intensity modulation. The 10W YAG laser (Lightwave model 220-1064-10000) has at least three

longitudinal modes that compete with one another causing instability in the frequency spectrum of the output beam. Therefore, we used a 700 mW-class NPRO type YAG laser (Lightwave model 220-1064-7000), which oscillates at a single longitudinal mode, as a probe laser for this measurement. To investigate the high power effect, we introduced the 10 W laser output with polarization orthogonal to that of the NPRO laser, so that it did not enter the photo-diode. The 10 W YAG laser beam was focused by a lens so that its radius at the EOM was the nominal value of 0.4 mm (10 ppm for the EOM aperture of 2 mm). Part of the beam was reflected by an optical wedge and was fed into an optical spectrum analyzer (Burleigh, model SA^{Plus}-200-XX) for monitoring the optical frequency spectrum The other part of the beam was fed into an RF photo-diode (EGG, FND-100) whose output was fed into an RF spectrum Analyzer (RFSA) and an oscilloscope, where the frequency spectrum and the total intensity were, respectively, measured. The EOM we tested was manufactured by New focus, Inc. (model 4003, broad band), and the modulation frequency was 21 MHz.

Figure 14: Experimental arrangement for sideband measurement.

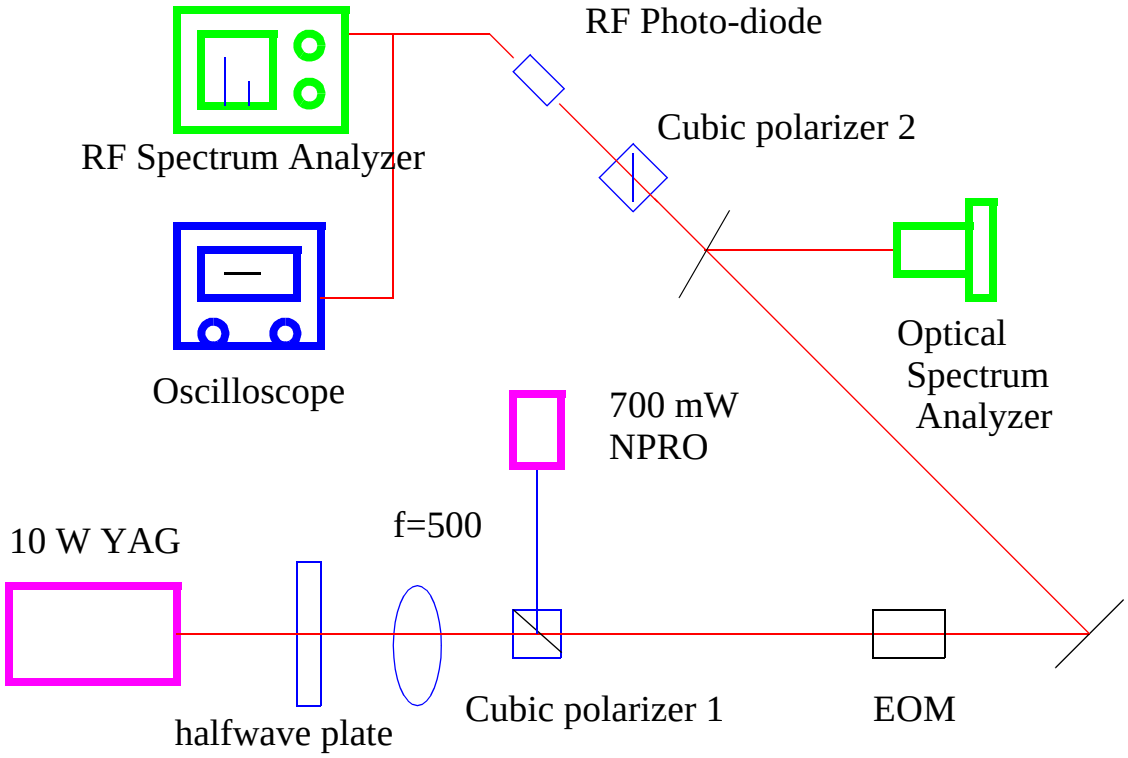

The residual intensity modulation is caused by misalignment of the angles between the incident polarization and the $LiNBO_3$'s crystallographic axis, and that between the $LiNBO_3$'s crystallographic axis and the orientation of the polarizer [8]. Depending on the initial phase retardation around which the modulation is applied, the intensity modulation observed in the RFSA has Ω component and 2Ω component at various ratios, where Ω is the modulation frequency. Thus in the following measurements, we monitored both components. In these measurements, the residual

intensity modulation is evaluated as the ratio of the Ω (2Ω) component of the RFSA signal (called the ac term) to the total intensity measured by the oscilloscope (called the dc term).

- Temporal variation of the residual intensity modulation at 10 W
- Power dependence of the residual intensity modulation
- Residual intensity modulation at various modulation depths
- Temperature dependence

4.2.1.1 Temporal variation

After careful alignment of the angles between the $LiNBO_3$'s crystallographic axis and the initial polarization/polarizer orientation, we exposed the EOM to 10 W and monitored the residual intensity modulation for over 2 hours. The modulation index of this measurement was 0.4. Figure 15 shows the result. Over the whole observation period, the Ω and 2Ω components stay within ± 20%.

Figure 15: Temporal variation of residual intensity modulation

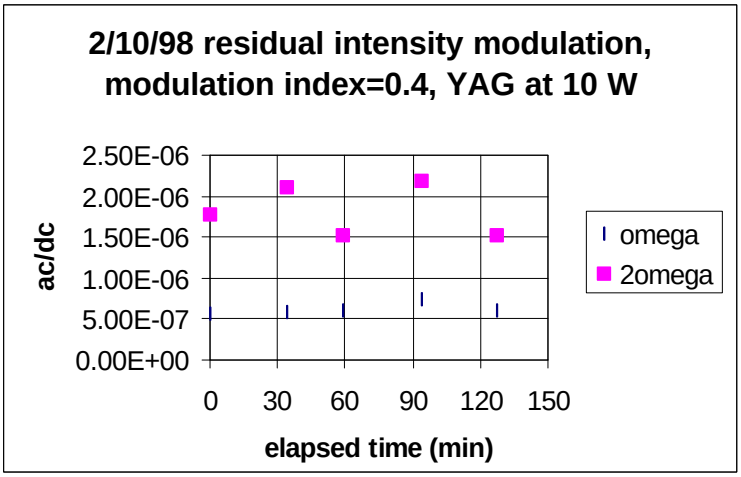

4.2.1.2 Power dependence

Figure 16 shows the influence of the superposed 10 W YAG laser power to the observed residual intensity modulation. The measurements were made after the $LiNBO_3$ crystal became thermally stable, which was checked by monitoring depolarization of the EOM (see below). *No substantial dependence on the YAG power is observed.*

Figure 16: Influence of YAG power to residual intensity modulation

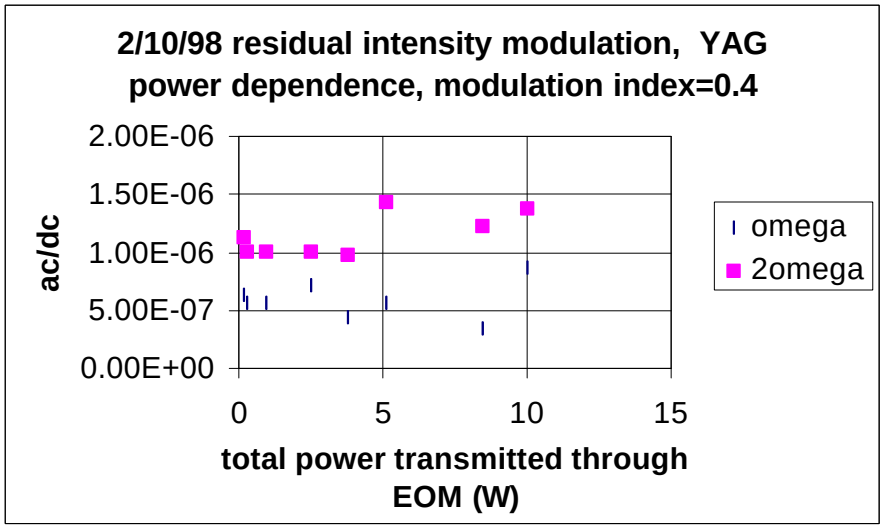

4.2.1.3 Residual intensity modulation at various modulation depths

We investigated temporal variation of the residual intensity modulation at lower modulation depths. Figure 17 and Figure 18 shows the results.

Figure 17: Influence of modulation depth to intensity modulation at Ω

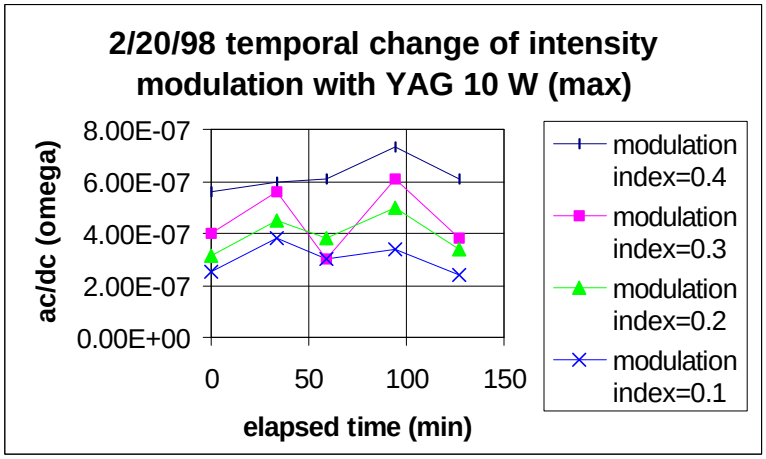

Figure 18: Influence of modulation depth to intensity modulation at 2Ω

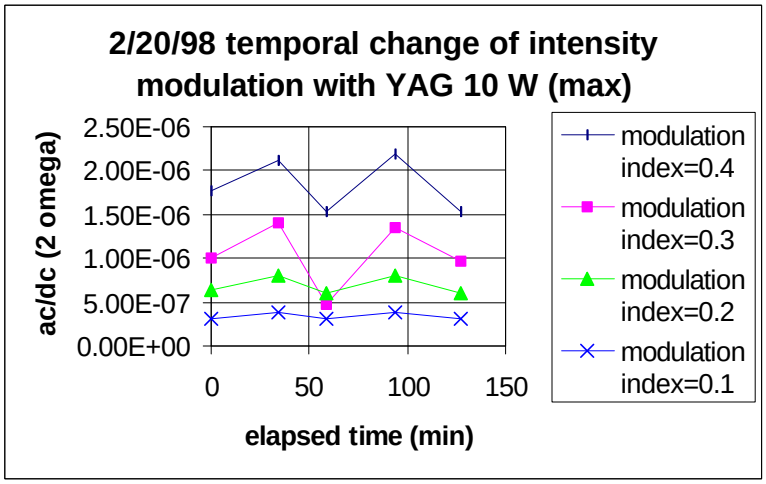

We also tested the residual intensity modulation at a higher modulation depth (modulation index = 1.1). This measurement was made after very careful alignment of the angles among the incident polarization, EOM's axis and the polarizer's orientation, and using the probe laser only. Figure 19 shows the result. The level of the intensity modulation is comparable to the case of the modulation index of 0.4.

Figure 19: Residual intensity modulation observed at a deeper modulation depth (modulation index=1.1)

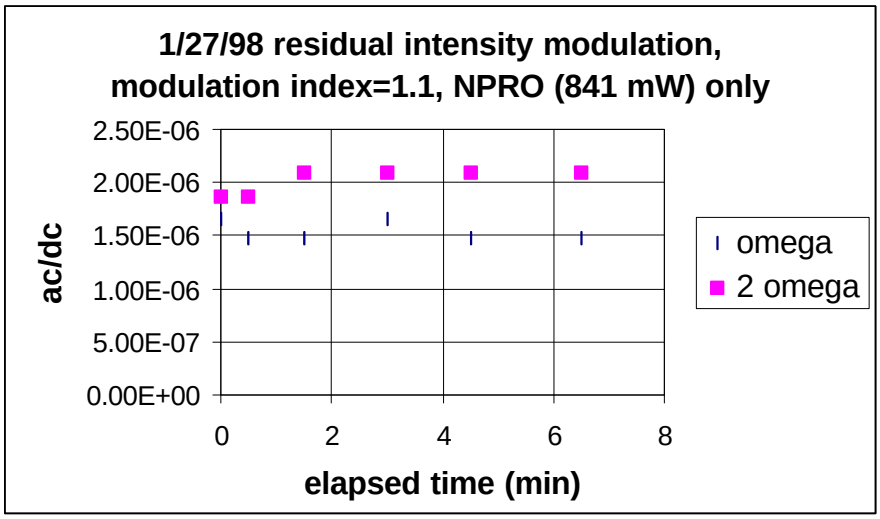

4.2.1.4 Temperature dependence

The residual intensity modulation depends on the initial phase retardation (between the ordinary light and extraordinary light) around which the modulation is applied. Since the refractive indices for ordinary light and extraordinary light of $LiNBO_3$ have very different temperature dependence, the residual intensity modulation is dependent on temperature. In fact, in the above measurements we observed that when high power YAG was superposed on the NPRO probe beam, the Ω and

2Ω components observed on the RFSA changed vigorously for the first some tens of minutes until the temperature of the crystal is stabilized. Thus above shown temporal variation of residual intensity modulation is considered to be caused by temperature fluctuation. Here we investigate the influence of ambient temperature on misaligned EOM. We changed the room temperature and measured the depolarization by the same setup as Figure 6. To enhance the depolarization, we intentionally misaligned the angle between the EOM's axis and the incident polarization. (The depolarization observed at a complete alignment is more than an order of magnitude lower, see Figure 23). The result is shown in Figure 20. Over the observation period of 60 min, we increased the room temperature approximately linearly by totally 4.5 °C and this caused the total phase retardation of 9 periods (9 x 2π).

Figure 20: Change in phase retardation of $LiNBO_3$ due to ambient temperature change

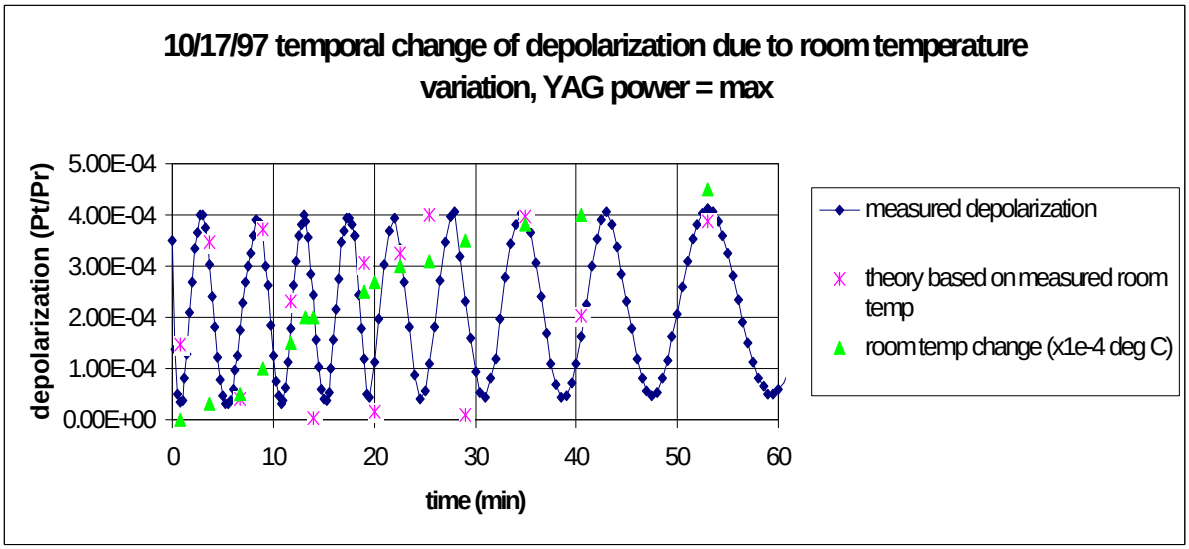

In Figure 20 we calculated the phase retardation by the formula shown below where Δϕ is the phase retardation, n_o is the refractive index of the ordinary light, n_e is the refractive index of the extraordinary light, T is the temperature, λ is the wavelength and L is the crystal length (4 cm).

$$\Delta\phi = \frac{2\pi}{\lambda}\{n_e(T) - n_O(T)\}L(T) \tag{5}$$

For each T, we evaluated n_e and n_o using the following formulas [9], and calculated Δϕ by eq.(10).

$$n_0^2 = 4.9130 + \frac{(1.173 \times 10^5 + 1.65 \times 10^{-2} T^2)}{(\lambda^2 - [212 + 2.7 \times 10^{-5} T^2]^2)} - 2.78 \times 10^{-8} \cdot \lambda^2 \quad (6)$$

$$n_e^2 = 4.5567 + 2.605 \times 10^{-7} T^2 + \frac{(0.970 \times 10^5 + 2.70 \times 10^{-2} T^2)}{(\lambda^2 - [201 + 5.4 \times 10^{-5} T^2]^2)} - 2.24 \times 10^{-8} \cdot \lambda^2 \quad (7)$$

where T is in K and λ is in nm. We used measured room temperature for T in the above equations. The measurement and calculation show reasonable agreement indicating that the observed change in depolarization is due to temperature change.

4.2.2. Damage Threshold/Thermal Lensing

4.2.2.1 Damage

We exposed the EOM to 10 W with the beam radius of 0.4 mm over 500 hours cumulatively. (The long-term exposure test is still ongoing). The transmission is a good indicator for a damage of the AR coating. So far, the initially measured transmission of 96±1% has not changed. Figure 21 shows power transmitted through the EOM as a function of cumulative exposure time.

Figure 21: YAG power transmitted through EOM

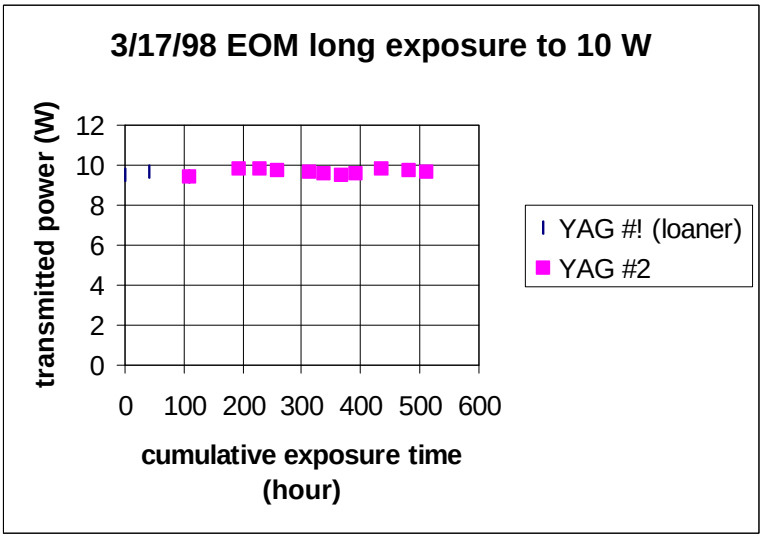

4.2.2.2 Thermal lensing

We measured thermal lensing in the EOM using the same setup as Figure 1. Figure 22 shows thermally induced change in the optical path length in a $LiNBO_3$ crystal.

Figure 22: Optical path length change by thermal lensing of EOM

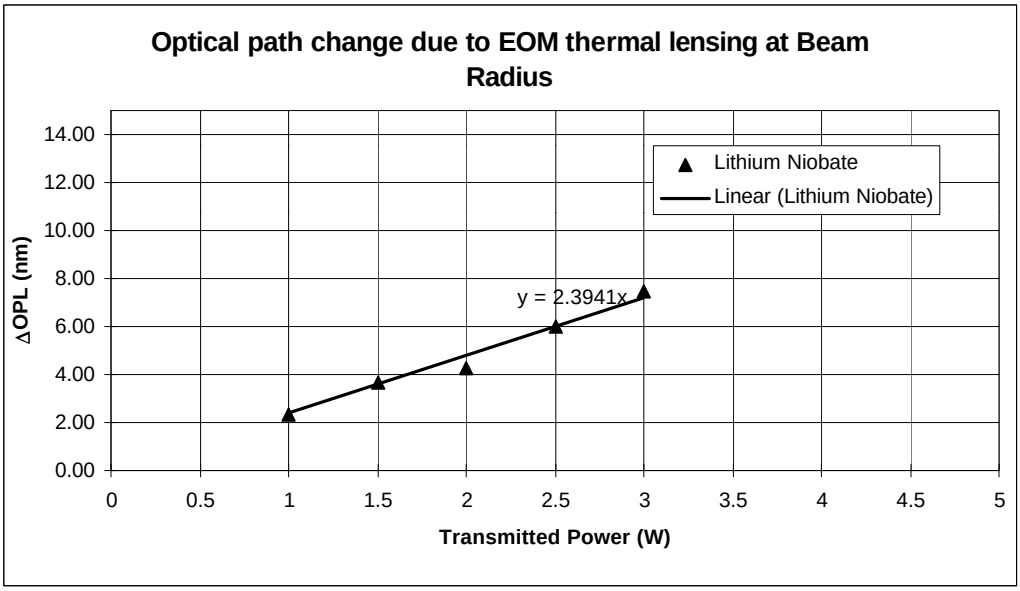

From the slope observed in Figure 22, the Optical path length change over the beam waist at 10 W can be estimated to be 24 nm. In the LIGO setup, the beam radius at the EOM is 0.4 mm. Thus the effective focal length F_{EOM} can be estimated from the following formula

$$F_{EOM} = \frac{r^2}{2\Delta OPL} \tag{8}$$

as $(0.4\text{x}10^{-3})^2/48\text{x}10^{-9}$=3.3 m. Since there are three EOMs in series, the overall thermal lens of the EOMs can be estimated approximately 1 m. This changes the waist of the beam after the EOMs from 0.397mm to 0.363 mm and shifts its location by 6.7 cm. These changes are compensatable by the mode matching telescope for the mode cleaner.

4.2.3. Alignment Tolerance

In order to make the intensity modulation lower than the required value of 10^{-3}, the misalignment in angle between the polarization and the EOM axis, and that between the polarization and the polarizer must be, respectively, less than 4 deg. Since this can be easily done, we examined how accurate we can align the angle. This was done by placing the EOM on a multi-axis stage having freedom of azimuthal rotation around the optical path, and monitoring the depolarization. Figure 23 shows the depolarization observed under the beast alignment we could achieve. Because of a random change in the ambient temperature, the depolarization varies as the time

elapses going through multiples of phase retardation of 2π as is the case of Figure 20. However, because of the better alignment, the amplitude of this temporal variation, $1.5x10^{-7}$, is two orders of magnitude lower than Figure 20. The misalignment estimated from eq.(3) is 0.02 deg.

Figure 23: Depolarization in EOM at best alignment

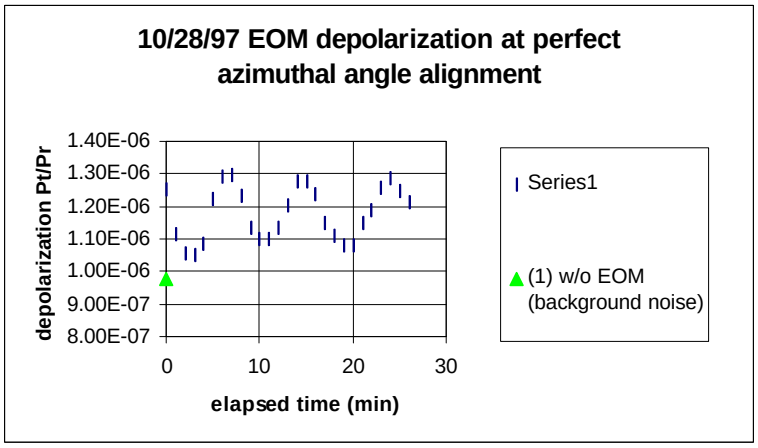

Table 7compares this best alignment with the alignment tolerance for the required residual intensity modulation.

Table 7: Alignment tolerance and best alignment achieved

alignment tolerance	*best alignment achieved*
4.3 deg	0.02 deg

4.3. EO Modulator Selection (Type, Manufacturer, etc.)

Table 8 shows the specifications of the selected EOM.

Table 8: EOM specifications

Manufacturer	*New focus, Inc.*
Model #	4003
Wavelength	1.0 - 1.6 μm
Type	Resonant Phase Modulator
Operating Frequency	ASC Resonant
Modulation depth	0.1 - 0.3 rad/V @ 1 μm
Max Vπ	10 - 31 V @ 1 μm

Table 8: EOM specifications

Material	$LiNbO_3$
Max Optical intensity	1 W/mm^2 (1.3 1 μm)
Aperture	2 mm
RF Bandwidth	2 - 4% freq.
Impedance	50 ohm
Max RF Power	55 mW

References:

[1] Input Optics Preliminary Design, 7.1.1.2, LIGO T970089-06-P, 8/28/97

[2] P. King, LIGO T970080-08-D, 6/6/97

[3] 3.2.1.4 optical isolation, T960093-02 pdf

[4] Justin Mansell, private communication, November, 1997. This is a simplified form of eq.(3) of K. A. Strain, K. Danzmann, J. Mizuno, P. G. Nelson, A. Rudiger, R. Schilling and W. Winkler, “Thermal lensing in recycling interferometric gravitational wave detectors,” Phys. Lett. A, vol. 194, pp. 124-132

[5] W. Winkler, A. Rudiger, R. Schilling, K. A. Strain and K. Danzmann, Birefringence-induced losses in interferometers, Opt. Com., 112, 245-252 (1994)

[6] Institute of Applied Physics, Private communication, Oct. 1997.

[7] P. Fritschel, G. Gonzalez, A. Marin, N. Mavalavala, D. Ouimette, L. Sievers, D. Sigg and M. Zucker, Length Sensing and Control Subsystem Preliminary Design, T970122-00D, 7/18/97

[8] S. Kawamura, A. Abramovici and M. E. Zucker, “Improved multistage wide band laser frequency stabilization”, Rev. Sci. Inst., Vol68, No.1, Pt.1, 223-229 (1997)

[9] Gmelins Handbuch der Anorganischen Chemie, N10B, teil B4, 58